ARCHIVES OF ELECTRICAL ENGINEERING VOL. 73(4), pp. 869–890 (2024)

DOI 10.24425/aee.2024.152100

# Study on model predictive control of dual three-phase permanent magnet synchronous motor based on biplane virtual voltage vector

HONG-YU TANG [1]✉, QU SHA [1], DE-ZHI XU [2]

[1] *School of Electrical and Information, Zhenjiang College*
*518 Chang Xiang xi road, Zhenjiang City, Jiangsu Province, China*
[2] *School of Electrical and Information Engineering, Jiangsu University*
*301 Xuefu Road, Zhenjiang City, Jiangsu Province, Zhenjiang 212013, China*
*e-mail:* ✉ *t_redrain@126.com, shaou@zjc.edu.cn, xudezhi@ujs.edu.cn*

(Received: 18.03.2024, revised: 12.11.2024)

**Abstract:** Under the traditional control method, the dual three-phase permanent magnet synchronous motor (DTP–PMSM) has a harmonic plane with low impedance, and it can produce larger harmonic current. Model predictive control (MPC) has a simple control structure and a good dynamic performance. The MPC is usually used in a high-performance control system of multiphase motors. Aiming at the DTP–PMSM drive system, an improved MPC strategy based on the biplane virtual voltage vector is proposed in this paper. In the proposed biplane MPC scheme, the voltage vector of the $\alpha$–$\beta$ plane is virtual to 25 voltage vectors, while the voltage vector of the $x$–$y$ plane is virtual to zero. At the same time, the voltage vector of the $x$–$y$ plane is virtual to 25 voltage vectors, while the voltage vector of the $\alpha$–$\beta$ plane is virtual to zero. On this basis, the cost function of the biplane is evaluated. The operating time and reference voltage of each vector are calculated. The virtual voltage vector on the $\alpha$–$\beta$ plane is used for electromechanical energy conversion to generate the best electromagnetic torque and reduce torque ripple. The virtual voltage vector on the $x$–$y$ plane is used to suppress the stator current harmonics and improve the efficiency of the DTP–PMSM. The simulation and experimental results demonstrate the superiority of the proposed biplane MPC.

**Key words:** biplane, double three-phase permanent magnet synchronous motor, harmonic current, model predictive control, virtual voltage vector

## 1. Introduction

In recent years, with the rapid development of social productivity, in many industrial driving fields, the reliability of a transmission system is required to be higher and higher, and the accuracy and rapidity of a control system are also required to be more and more strict. Compared with the traditional three-phase motor, the double three-phase motor has the advantages of large output power, small torque ripple, high power density and strong fault tolerance. It has been more and more widely used in the fields of electric aircraft, automobiles, and ship propulsion [1]. Common control strategies for polyphase motors mainly include vector control based on vector space decoupling, direct torque control and model predictive control [2, 3]. The vector control is similar to the vector control of a three-phase motor. The $\alpha$–$\beta$ plane uses 12 maximum vectors of the outermost layer as the basic voltage vectors. This control method can obtain the maximum voltage utilization of the inverter DC bus [4]. However, the method ignores the harmonic plane of the polyphase motor, resulting in many harmonics in the stator current of the polyphase motor, which reduces the operating efficiency of the motor system. In addition, the vector voltage is unique in the cycle, which has the disadvantages of large fluctuations in flux linkage and torque ripple [5].

Model predictive control (MPC) has the advantages of simple control unit structure, fast response speed and easy-to-handle multivariable optimal control. It is widely used in polyphase motors [6, 7]. However, the traditional MPC only performs optimal control in the fundamental wave plane involved in energy exchange, and only the voltage vector on the $\alpha - \beta$ plane is considered [8], but the harmonic loss caused by the nonlinear factors of the system is not fully considered [9]. Due to the low impedance on the harmonic $x$–$y$ plane, the harmonic voltage in the phase voltage, especially the 5th and 7th harmonic voltage, will produce large harmonic current on the $x$–$y$ plane, so the control effect is not ideal [10]. Scholars have conducted in-depth research in the fields. The common mode voltage suppression method based on a virtual vector inverter model is proposed to achieve common mode voltage suppression and reduce current harmonics at the same time [11, 12]. On the $\alpha$–$\beta$ plane, the maximum vector and the sub-large vector are used to synthesize one reference voltage vector, and then the sub-large vector and the small vector are used to synthesize another reference voltage vector [13–15]. During the synthesis process, this method can ensure that the mapping voltage amplitude of the $x$–$y$ plane is 0, and this method can improve utilization ratio of the voltage vector on the $\alpha$–$\beta$ plane. But the voltage vector amplitude is fixed and cannot be adjusted, the motor phase current still contains harmonic components [16, 17]. On the $\alpha$–$\beta$ plane, the best in-phase voltage vector closest to the reference voltage vector is selected as the prediction vector to optimize the torque and flux regulation effect of the motor, reducing the torque ripple of the motor [18, 19]. However, the above torque control is only limited to single-plane control. In essence, the $x$–$y$ plane is still open-loop control [20, 21]. If the inverter dead time effect and system nonlinear factors are considered, the voltage vector on the $x$–$y$ harmonic sub-plane cannot be offset to 0. Therefore, there are still large current harmonics in the single-plane control, which increases the harmonic loss and reduces the system efficiency [22]. The double-plane control method is required to improve the control performance of the DTP–PMSM system.

This paper proposes a biplane MPC scheme with 25 virtual voltage vectors. The proposed scheme makes full use of the voltage vectors on the $\alpha$-$\beta$ and $x$–$y$ planes. In the $\alpha$–$\beta$ plane, the large and medium-large vectors are combined into 12 virtual voltage vectors, the medium-large and small vectors are combined into 12 virtual voltage vectors, plus zero vectors, that is, a total

of 25 virtual voltage vectors. Using a similar approach, 25 virtual voltage vectors can also be obtained in the $x$–$y$ plane. Compared with the single-plane MPC strategy, the proposed biplane MPC strategy can better suppress the harmonic currents. The simulation system and test platform are built. The simulation and experimental results show that the proposed biplane MPC scheme can reduce current harmonics, improve torque performance and system efficiency.

## 2. Driving topology and mathematical model of DTP–PMSM

### 2.1. Driving topology of DTP–PMSM

The DTP–PMSM is also called an asymmetric six-phase PMSM. The phase band angle of the motor is 30 degrees. Like the symmetrical twelve phase motor, the stator winding of the DTP–PMSM is connected to the six bridge arms of the inverter respectively. The driving topology is shown in Fig. 1.

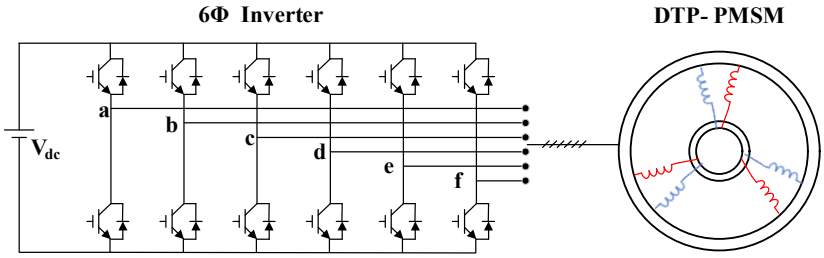


Fig. 1. DTP–PMSM drive topology

Because the phase band angle of the DTP–PMSM is 30 degrees, it can eliminate the 5th and 7th harmonic magnetic potential within the motor, thus eliminating the 6th torque ripple, and increasing the minimum number of torque ripple to 12 times. Therefore, the DTP–PMSM can effectively suppress the torque ripple and has been widely used in industrial production.

### 2.2. Mathematical model of DTP–PMSM

The six-phase inverter can be regarded as two three-phase inverters with isolated neutral points in parallel. The inverter consists of six bridge arms, and each bridge arm contains two power switching devices. The output state of the bridge arm of the six-phase inverter can be expressed by the vector $[S]$, $[S] = \{S_a, S_b, S_c, S_d, S_e, S_f\}$. Where $S_a$, $S_b$, $S_c$, $S_d$, $S_e$ and $S_f$, respectively, represent the switch states of the six bridge arms. If the upper bridge arm is on and the lower bridge arm is off, it is 1, otherwise it is 0.

Therefore, the six-phase inverter has $2^6 = 64$ switching states [23, 24]. Similar to the three-phase motor, the vector decoupling method is usually used to analyze the mathematical model of the double three-phase motor. The Clarke transform is performed on the double three-phase motor to map the motor variables to the $\alpha$–$\beta$ sub-plane, $x$–$y$ sub-plane and $o_1$–$o_2$ sub-plane, and the three sub-planes are orthogonal to each other. The static transformation matrix $T_{6S}$ of the dual three-phase motor is shown in Eq. (1).

$$T_{6S} = \frac{1}{3}\begin{bmatrix} 1 & -\frac{1}{2} & -\frac{1}{2} & \frac{\sqrt{3}}{2} & -\frac{\sqrt{3}}{2} & 0 \\ 0 & \frac{\sqrt{3}}{2} & -\frac{\sqrt{3}}{2} & \frac{1}{2} & \frac{1}{2} & -1 \\ 1 & -\frac{1}{2} & -\frac{1}{2} & -\frac{\sqrt{3}}{2} & \frac{\sqrt{3}}{2} & 0 \\ 0 & -\frac{\sqrt{3}}{2} & \frac{\sqrt{3}}{2} & \frac{1}{2} & \frac{1}{2} & -1 \\ 1 & 1 & 1 & 0 & 0 & 0 \\ 0 & 0 & 0 & 1 & 1 & 1 \end{bmatrix}, \tag{1}$$

where the first two lines of Eq. (1) map the fundamental wave and $12k \pm 1$ ($k = 1, 2, 3, \ldots$) subharmonic of the motor to the $\alpha$-$\beta$ sub-plane. The $\alpha$–$\beta$ sub-plane is consistent with the air gap flux rotation plane of the motor, so the current component on the $\alpha$–$\beta$ sub-plane participates in the electromechanical energy conversion process. The middle two lines of Eq. (1) map the $6k \pm 1$ ($k = 1, 3, 5, \ldots$) sub-harmonic of the motor to the $x$–$y$ sub-plane, and the last two lines of Eq. (1) map the $6k \pm 3$ ($k = 1, 3, 5, \ldots$) sub-harmonic of the motor to the $o_1$–$o_2$ sub-plane. Since the $x$–$y$ sub-plane and $o_1$–$o_2$ sub-plane are orthogonal to the air-gap flux rotation plane of the motor, the current components on the $x$–$y$ and $o_1$–$o_2$ sub-planes do not generate rotating magnetic potential, and the current components on the two planes do not participate in the electromechanical energy conversion process. If the neutral points of two parallel three-phase inverters are isolated from each other in the driving system of the DTP–PMSM, the zero-sequence current component of the three-phase inverter on the $o_1$–$o_2$ sub-plane is therefore 0, as long as the zero-sequence current component on the $x$–$y$ sub-plane is controlled to ensure that their vector sum is 0.

According to the Clarke–Park total transformation matrix $T_{6S}$, the torque equation of the DTP–PMSM can be obtained as shown in Eq. (2).

$$T_e = 3p_n(\psi_d i_q - \psi_q i_d), \tag{2}$$

where $i_d$, $i_q$, $\psi_d$, $\psi_d$ represent the components of stator current and flux linkage on the $dq$-axis, respectively, and $p_n$ represents the pole pairs of the motor.

## 3. Biplane virtual voltage vector

### 3.1. Space voltage vector of six phase inverter

Since the six-phase inverter has a total of 64 switch states, each switch state is mapped to voltage vectors on the $\alpha$–$\beta$ sub-plane and the $x$–$y$ sub-plane can be expressed as follows:

$$u_{\alpha\beta} = \frac{1}{3}U_{dc}(S_a + S_b e^{j120^\circ} + S_c e^{j240^\circ} + S_d e^{j30^\circ} + S_e e^{j150^\circ} + S_f e^{j270^\circ}), \tag{3}$$

$$u_{xy} = \frac{1}{3}U_{dc}(S_a + S_b e^{j240^\circ} + S_c e^{j120^\circ} + S_d e^{j150^\circ} + S_e e^{j30^\circ} + S_f e^{j270^\circ}), \tag{4}$$

where $v_\alpha$ and $v_{xy}$, respectively, represent mapping to the space voltage vector on the $\alpha$–$\beta$ sub-plane and $x$–$y$ sub-plane, and $U_{dc}$ represents the DC bus voltage of the inverter. According to Eqs. (3) and (4), 64 switching states of the six-phase inverter can be drawn. The space voltage vector graph of the $\alpha$–$\beta$ sub-plane and $x$–$y$ sub-plane is shown in Fig. 2.

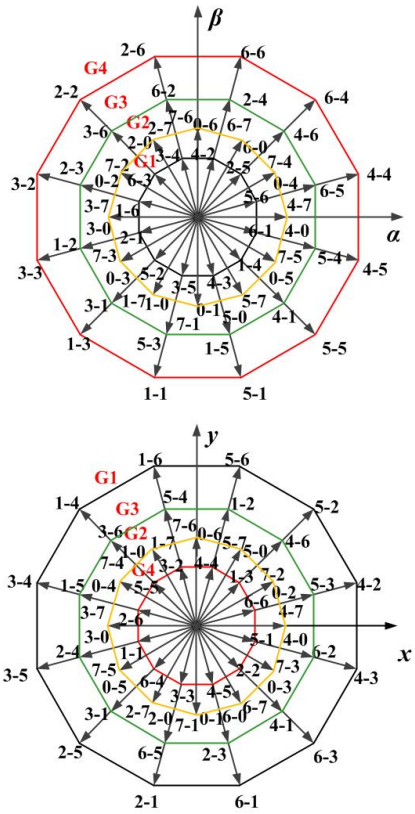


Fig. 2. Space voltage vector graph of $\alpha$–$\beta$ sub-plane and $x$–$y$ sub-plane

In Fig. 2, each voltage vector is represented by an octal number, and a group of binary numbers corresponding to the octal number represents a switching state. For example, "3–4" represents the switching state (011100), that is, the upper bridge arms of $b$, $c$ and $d$ are on, and the rest of the bridge arms are off. Each plane contains 48 effective vectors, corresponding to 60 switching states, respectively, and 4 zero vectors, corresponding to the switching states "0–0, 0–7, 7–0, 7–7". According to the grouping of voltage vectors, the 48 effective voltage vectors can be divided into 4 regular dodecagons, which are composed of 12 large vectors, 12 medium large vectors, 12 medium vectors and 12 small vectors, respectively.

### 3.2. Biplane virtual voltage vector synthesis

In order to improve the rapidity and effectiveness of MPC and reduce the calculation time of the control system, only part of the effective vector can be used to calculate the virtual voltage vector in biplane synthesis. The traditional method is to use the phase difference 180° on the $x$–$y$ sub-plane between the large and the medium-large vector of the $\alpha$–$\beta$ sub-plane. The large and medium-large vectors of the $\alpha$–$\beta$ sub-plane are synthesized by the virtual voltage vector in a certain proportion. The virtual voltage vector is zero on the $x$–$y$ sub-plane, which can not only

offset the harmonic current, but also find the reference voltage vector quickly and accurately. According to this method, a total of 12 virtual voltage vectors can be synthesized, plus zero vectors, a total of 13 vectors, called VV13. The VV13 control method only uses 24 effective voltage vectors and zero vectors, and does not make full use of 64 switch states in the plane. In order to improve the control accuracy and make full use of the switching state of the inverter, the large vector and the medium-large vector are synthesized into 12 virtual voltage vectors, and the medium-large vector and the small vector are combined into 12 virtual voltage vectors. With an additional plus zero vector, there are 25 vectors in total, which is called VV25.

VV25 makes full use of the space voltage vector and improves the DC voltage utilization of the six-phase inverter. However, only setting the proportional synthesis vector cannot completely suppress the harmonic voltage on the $x$–$y$ sub-plane. Since the impedance on the $x$–$y$ sub-plane is very small, and a small harmonic voltage vector can also generate a large harmonic current on the $x$–$y$ sub-plane, the idea of biplane prediction can be introduced. 25 virtual voltage vectors are synthesized in the $\alpha$-$\beta$ sub-plane to generate the required magnetic flux and torque. 25 virtual voltage vectors are synthesized in the $x$–$y$ sub-plane to suppress harmonic current, and improve the accuracy and stability of motor control, achieving good control effect.

From Fig. 2, medium and large vectors $v_{4-6}$ are in phase with large vectors $v_{6-4}$ and small vectors $v_{2-5}$ in the $\alpha$–$\beta$ sub-plane, but medium and large vectors $v_{4-6}$ are in phase with large vectors $v_{6-4}$ and small vectors $v_{2-5}$ in the $x$–$y$ sub-plane. Therefore, on the $x$–$y$ sub-plane, the flux linkage generated by medium and large vectors $v_{4-6}$ is also reversed from that generated by large vectors $v_{6-4}$ and small vectors $v_{6-4}$. In order to suppress the current harmonics on the $x$–$y$ sub-plane, it is only necessary to offset the large vector, medium-large vector and small vector to 0 on the $x$–$y$ sub-plane to reduce the harmonic current. According to the magnitude of each vector on the $\alpha$–$\beta$ sub-plane, the action time of the large vector, medium large vector and small vector can be calculated, as shown in Eqs. (5)–(8).

$$vv_i = t_1 v_{\mathrm{large}} + t_2 v_{\mathrm{medium-large}}, \tag{5}$$

$$t_1 v_{\mathrm{small}} + t_2 v_{\mathrm{medium-large}} = 0, \tag{6}$$

$$vv_{i+12} = t_3 v_{\mathrm{medium-large}} + t_4 v_{\mathrm{small}}, \tag{7}$$

$$t_3 v_{\mathrm{medium-large}} + t_4 v_{\mathrm{large}} = 0, \tag{8}$$

where: $vv_i$ and $vv_{i+12}$ are the synthetic virtual voltage vectors, $t_1$ and $t_2$ are the synthetic action time of the large vector and medium-large vector, $t_3$ and $t_4$ are the synthetic action time of the medium-large vector and small vector. $v_{\mathrm{large}}$, $v_{\mathrm{medium-large}}$ and $v_{\mathrm{small}}$ are the amplitudes of the large vector, medium-large vector and small vector, respectively. According to Eqs. (5)–(8), $t_1 = 0.73T_s$, $t_2 = 0.27T_s$, $t_3 = 0.58T_s$, and $t_4 = 0.42T_s$ can be calculated, where $T_s$ is the sampling period. The synthetic virtual voltage vector graph of the $\alpha$–$\beta$ sub-plane is shown in Fig. 3.

Similarly, on the $x$–$y$ sub-plane, the large vector and the medium-large vector are synthesized into 12 virtual voltage vectors, and the medium-large vector and the small vector are synthesized into 12 virtual voltage vectors. The component of the virtual voltage vectors on $\alpha$–$\beta$ the sub-plane is 0, and the action time of each vector is calculated. The calculation method is the same as that described above. The synthetic virtual voltage vector graph of the $x$–$y$ sub-plane is shown in Fig. 4.

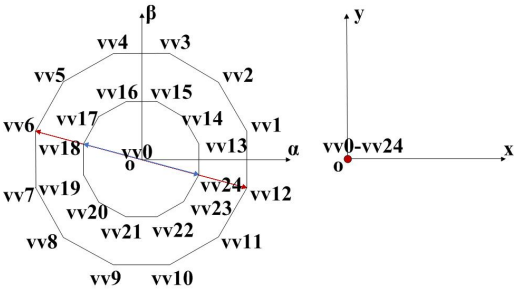


Fig. 3. Synthetic virtual voltage vector graph of the $\alpha$–$\beta$ sub-plane

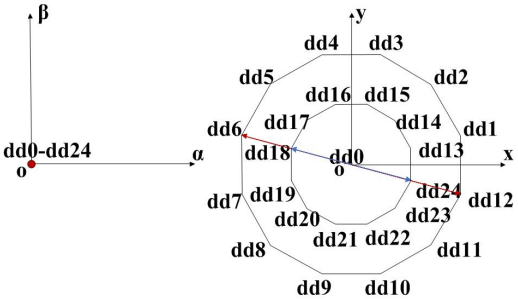


Fig. 4. Synthetic virtual voltage vector graph of the $x$–$y$ sub-plane

## 4. Biplane virtual voltage vector MPC

### 4.1. Cost function

Considering that the electromagnetic torque is controlled on the $\alpha$-$\beta$ sub-plane and the harmonic current is suppressed on the $x$–$y$ sub-plane, the cost function $g$ of the DTP–PMSM can be expressed by Eq. (9).

$$\begin{cases} g_1 = |i_\alpha^* - i_\alpha(k+1)| + |i_\beta^* - i_\beta(k+1)| \\ g_2 = |i_x^* - i_x(k+1)| + |i_y^* - i_y(k+1)| \end{cases}, \tag{9}$$

where $i_\alpha, i_\beta, i_\alpha^*, i_\beta^*$ are the reference current and $k+1$ order prediction current of the $\alpha$–$\beta$ sub-plane, respectively. $j_x, i_y, i_x^*, i_y^*$ are the reference current and $k+1$ order prediction current of the $x$–$y$ sub-plane, respectively.

### 4.2. Reference voltage vector calculation

Using the forward Euler formula, the discrete model of the DTP–PMSM can be derived, and the $k$-order voltage of the $dq$-axis on the $\alpha$–$\beta$ sub-plane is expressed by $v_d(k)$ and $v_q(k)$, and the calculation method is shown in Eq. (10).

$$\begin{cases} v_d(k) = R_s i_d(k) + \dfrac{L_d}{T_s}\left(i_d(k+1) - i_d(k)\right) \\ v_q(k) = R_s i_q(k) + \dfrac{L_q}{T_s}(i_q(k+1) - i_q(k)) + \omega_e \lambda_f \\ v_x(k) = R_s i_x(k) + \dfrac{L_d}{T_s}(i_x(k+1) - i_x(k)) \\ v_y(k) = R_s i_y(k) + \dfrac{L_q}{T_s}(i_y(k+1) - i_y(k)) \end{cases}, \tag{10}$$

where $i_d(k)$, $i_d(k+1)$, $i_q(k)$, $i_q(k+1)$ are the $k$ order and $k+1$ order predictive current of the $dq$-axis, respectively. $e_d$ and $e_q$ are the back EMF of the $dq$-axis, respectively. In order to compensate the control delay, the $k+2$ order predictive current value of the $dq$-axis can be further calculated according to the Euler discrete formula, as shown in Eq. (11).

$$\begin{cases} i_d(k+2) = \left(1 - \dfrac{R_s T_s}{L_d}\right) i_d(k+1) + \dfrac{L_q}{L_d}\omega_e T_s i_q(k+1) + \dfrac{T_s}{L_d} v_d(k+1) \\ i_q(k+2) = \left(1 - \dfrac{R_s T_s}{L_q}\right) i_q(k+1) - \dfrac{L_d}{L_q}\omega_e T_s i_d(k+1) + \dfrac{T_s}{L_q} v_q(k+1) - \dfrac{\omega_e \lambda_f T_s}{L_q} \\ i_x(k+2) = \left(1 - \dfrac{R_s T_s}{L_0}\right) i_x(k+1) + \dfrac{T_s}{L_0} u_x(k+1) \\ i_y(k+2) = \left(1 - \dfrac{R_s T_s}{L_0}\right) i_y(k+1) + \dfrac{T_s}{L_0} u_y(k+1) \end{cases}. \tag{11}$$

According to the $dq$-axis reference currents, $i_d^{\text{ref}}$ and the $k+2$ order predicted current value, the reference voltage values $v_d^{\text{ref}}$ and $v_q^{\text{ref}}$ of the $dq$-axis can be calculated, as shown in Eq. (12).

$$\begin{cases} v_d^{\text{ref}} = R_s i_d(k+2) + \dfrac{L_d}{T_s}\left(i_d^{\text{ref}} - i_d(k+2)\right) \\ v_q^{\text{ref}} = R_s i_q(k+2) + \dfrac{L_q}{T_s}\left(i_q^{\text{ref}} - i_q(k+2)\right) + \omega_e \lambda_f \end{cases}. \tag{12}$$

Finally, according to the values of the reference voltages $v_d^{\text{ref}}$ and $v_q^{\text{ref}}$, the reference voltage amplitude and phase angle are calculated, the sector of the reference voltage is determined, and the appropriate virtual composite voltages $vv_i$ and $vv_{i+12}$ are selected.

Similarly, on the $x$–$y$ sub-plane, the $k$ order voltage of the $dq$-axis can be calculated according to the discrete model of the motor. Since it is necessary to suppress torque ripple on the $x$–$y$ plane, the sum of the $dq$-axis reference current on the $x$–$y$ plane should be 0. According to Eq. (13), the reference voltage values $i_x^{\text{ref}}$ and $i_y^{\text{ref}}$ of the $dq$-axis on the $x$–$y$ plane can be calculated as follows:

$$\begin{cases} v_x^{\text{ref}} = R_s i_x(k+2) + \dfrac{L_0}{T_s}(i_x^{\text{ref}} - i_x(k+2)) \\ v_y^{\text{ref}} = R_s i_y(k+2) + \dfrac{L_0}{T_s}(i_y^{\text{ref}} - i_y(k+2)) \end{cases}. \tag{13}$$

### 4.3. Control block diagram

The MPC block diagram based on the vector of biplane virtual voltage is shown in Fig. 5.

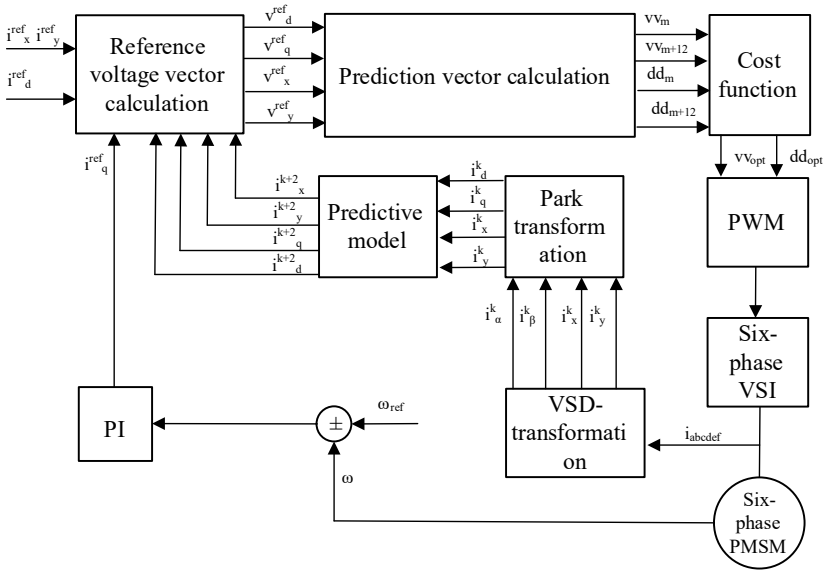


Fig. 5. MPC block diagram based on vector of biplane virtual voltage

The 6-phase current of the DTP–PMSM is transformed by variable-speed driver and Clarke Park coordinate transformation. The $k+2$ order prediction currents $i_x^{k+2}$, $i_y^{k+2}$, $i_q^{k+2}$ and $i_d^{k+2}$ are calculated in the $\alpha$–$\beta$ and $x$–$y$ sub-plane. After comparing with the reference currents, then through the inversion matrix and prediction model, the reference voltage vectors $vv_m$, $vv_{m+12}$, $dd_m$, $dd_m$, $dd_{m+12}$ can be obtained in the two planes. Through the cost function, the optimal synthetic voltage vector is selected on two planes respectively, and the motor is driven to run after PWM conversion.

## 5. Simulation and experimental verification

### 5.1. Simulation verification

In order to prove the correctness of the method proposed in this paper, the simulation is carried out in the MATLAB/Simulink environment. Table 1 shows the simulation parameters of the DTP–PMSM. The simulation results are shown in Fig. 6 and Fig. 7. Figure 6(a), Fig.6(b), and Fig. 6(c) show the steady-state waveforms of VV13, VV25 and VV25-Bi. Figure 7(a), Fig. 7(b), and Fig. 7(c) show the dynamic waveforms of VV13, VV25 and VV25-Bi.

Firstly, the steady-state performance is studied at a motor speed of 400 r/min and $T_e$ being 15 N·m. It can be found from Fig. 6 that the phase current waveform of the VV25-Bi MPC is more sinusoidal than the VV13 MPC and VV25 MPC strategies, which indicates that the proposed control strategy achieves better harmonic suppression, thus improving the efficiency of the DTP–PMSM drive system.

Table 1. Simulation parameters of DTP–PMSM

| Motor parameters | Numerical value |
|---|---|
| $Q$-axis inductance (mH) | 2.46 |
| $D$-axis inductance (mH) | 2.46 |
| Zero axis inductance (mH) | 0.52 |
| Stator resistance (Ω) | 0.67 |
| Polar logarithm (Pn) | 5 |
| Rotor flux linkage (Wb) | 0.0885 |
| Rated speed (r/min) | 400 |
| Rated torque (N·m) | 30 |
| Sampling frequency (kHz) | 10 |
| Switching frequency (kHz) | 10 |
| DC bus voltage (V) | 100 |
| Dead time (μs) | 2 |

Secondly, the dynamic performance of the motor, where the load torque reference has a step change from 15 N.m to 30 N.m is shown in Fig. 7 and from 0 N.m to 15 N.m in Fig. 8 at the time 0.1 s, respectively. It can be seen from Fig. 7 and Fig. 8 that the VV13, VV25, and VV25-Bi methods have similar dynamic response with fast torque response and less overshoot. When sudden load is applied, the motor speed drops less. In addition, a step change from 200 to 400 r/min is applied to the DTP–PMSM in the speed command, as shown in Fig. 9. It can be seen that the three methods have similar dynamic response.

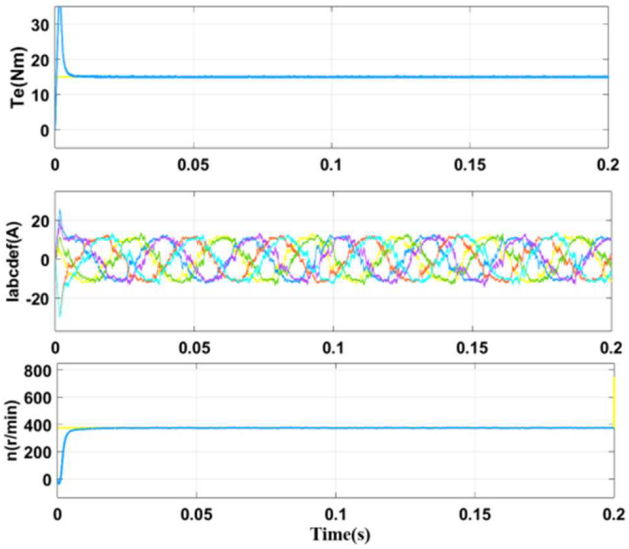


(a) VV13

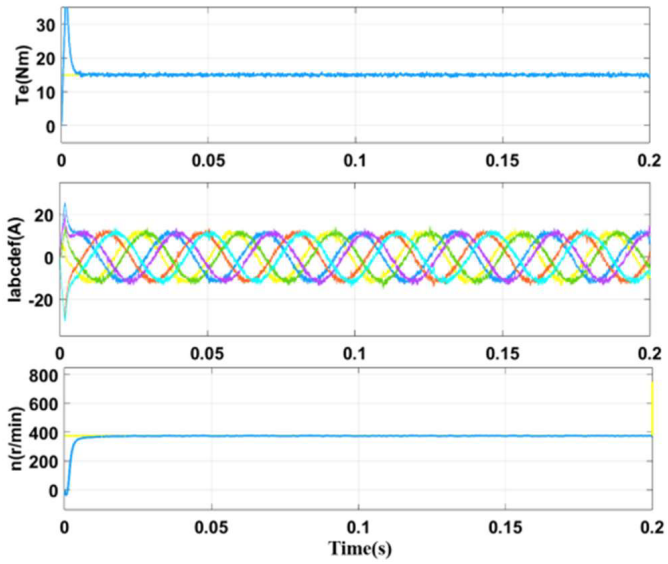


(b) VV25

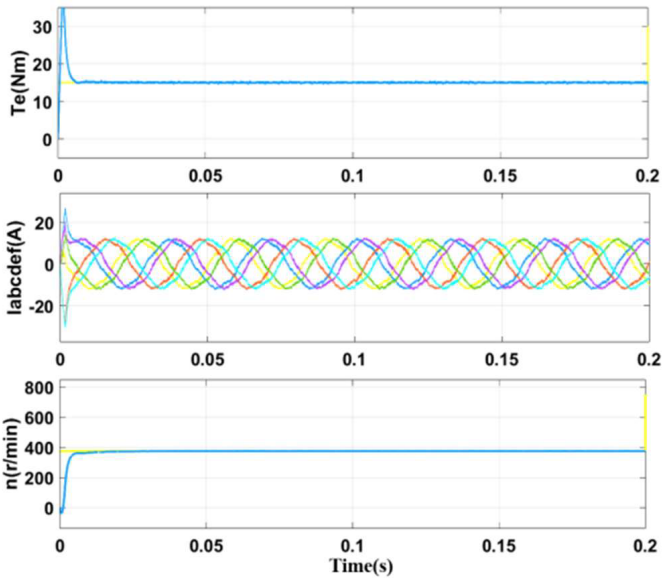


(c) VV25-Bi

Fig. 6. Steady state waveform of the three MPC strategies

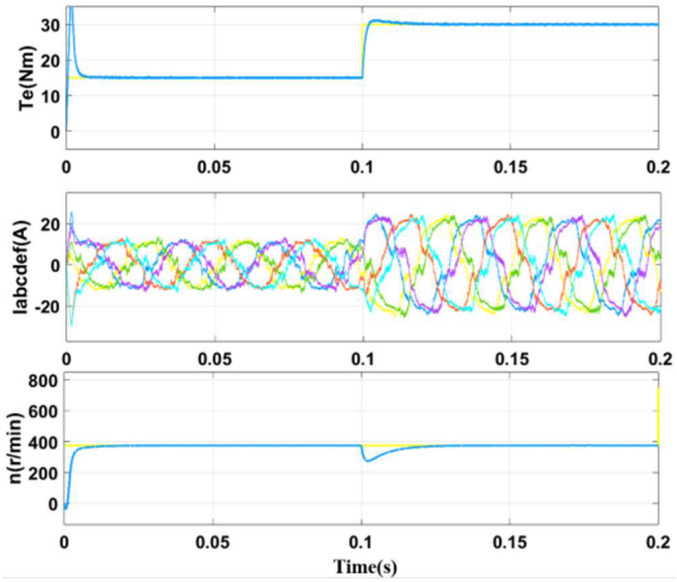


(a) VV13

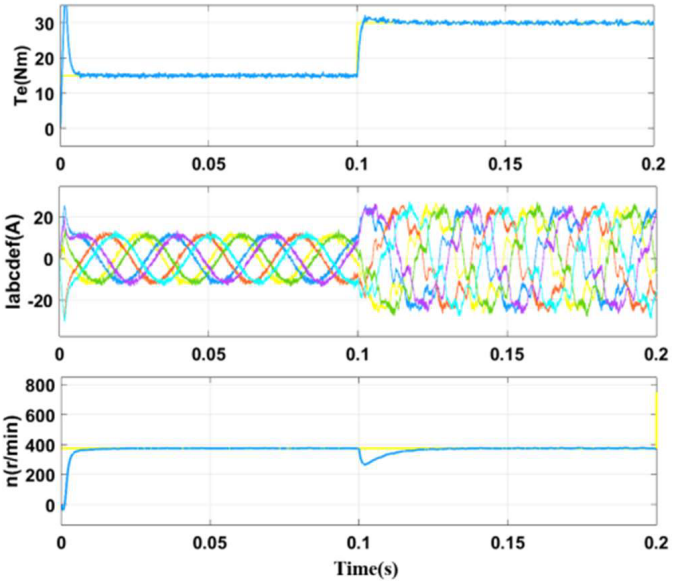


(b) VV25

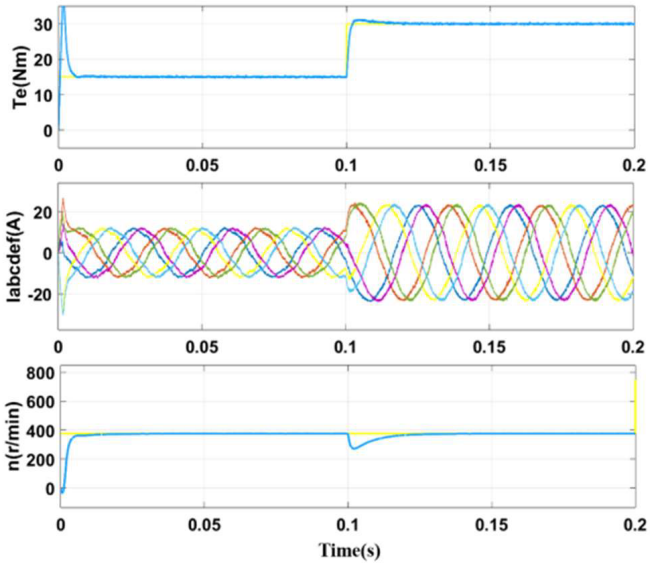


(c) VV25-Bi

Fig. 7. Dynamic waveform of the three MPC strategies under the half-load to full-load step response

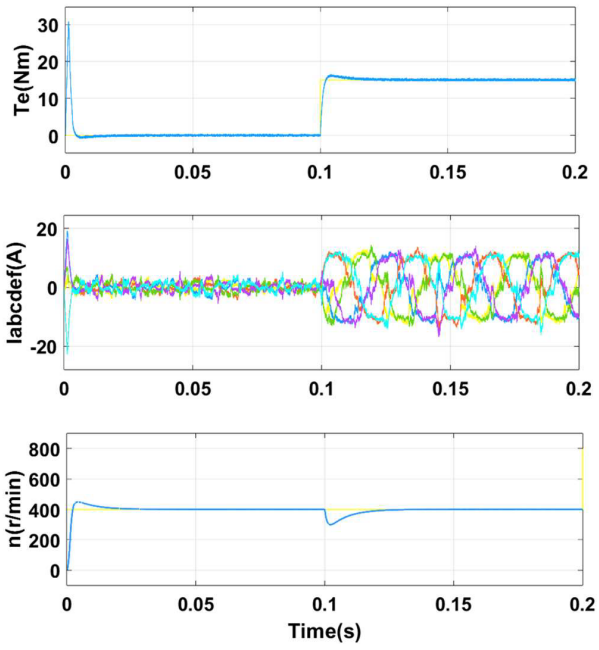


(a) VV13

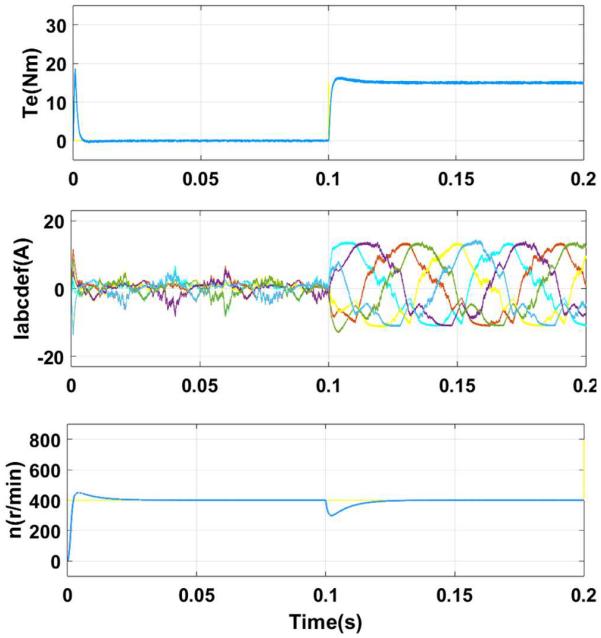


(b) VV25

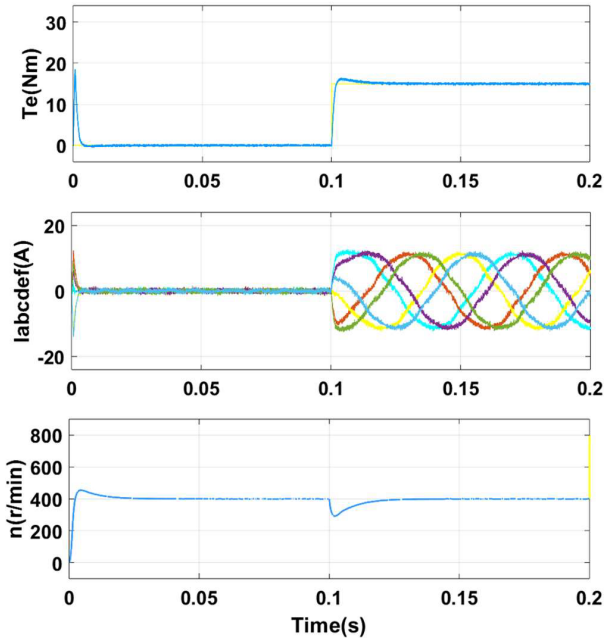


(c) VV25-Bi

Fig. 8. Dynamic waveform of the three MPC strategies under the no-to-half-load step response

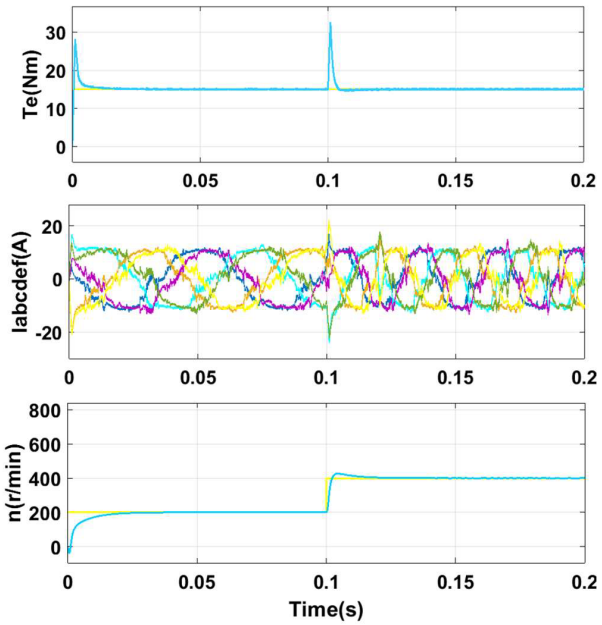
Te(Nm)
30
20
10
0
0
0.05
0.1
0.15
0.2
labcdef(A)
20
0
-20
n(r/min)
800
600
400
200
Time(s)

(a) VV13

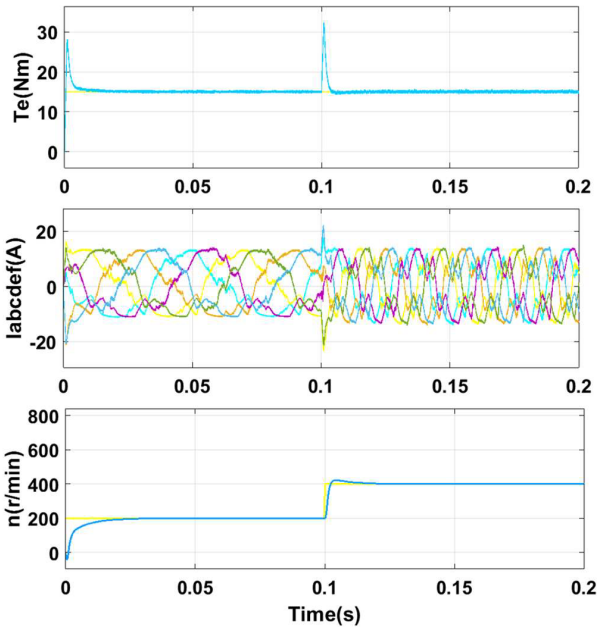
Te(Nm)
30
20
10
0
0
0.05
0.1
0.15
0.2
labcdef(A)
20
0
-20
n(r/min)
800
600
400
200
Time(s)

(b) VV25

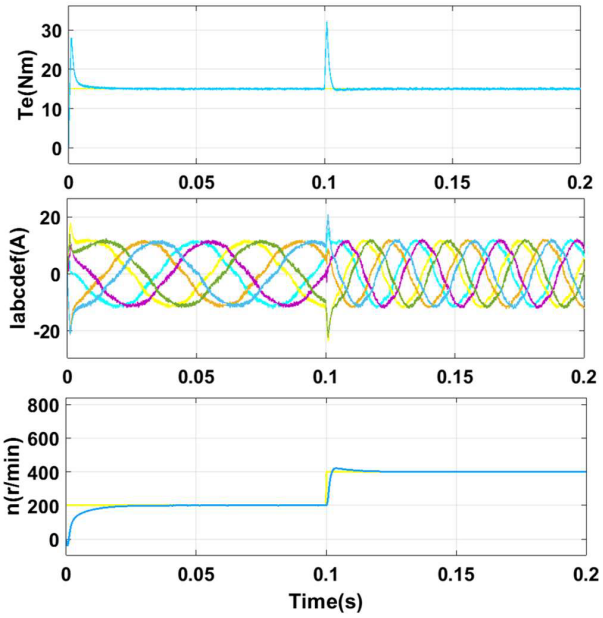


(c) VV25-Bi

Fig. 9. Dynamic waveform of the three MPC strategies under the speed step response

## 6. Experimental verification

In order to verify the correctness of the proposed method, a DTP–PMSM experimental platform is built. The experimental platform consists of the DTP–PMSM, the load, the six-phase voltage source inverter, and the DC power supply. The six-phase voltage source inverter is built with discrete IGBT devices. A floating-point digital signal processor (TMS320F28377S) is chosen to execute the proposed algorithm. The CPLD is used for hardware logic protection. The load of the DTP–PMSM is a three-phase PMSM with a three-phase resistance load, where the per-phase resistance is 20 Ω. Figure 10 shows the structure of the experimental platform. First, connect the DC power supply to the DC side of the dual three-phase inverter, connect the AC side of the dual three-phase inverter to the dual three-phase motor, drive the load through the three-phase load motor, and record the voltage, speed, torque, and other experimental data of the DTP–PMSM through the oscilloscope.

First, we used the experimental platform to test the steady-state performance of the DTP–PMSM. The motor experimental waveform at the speed of 360 r/min is shown in Fig. 11. Figure 11(a) is the waveform under the VV13 method and Fig. 11(b) is the waveform under the VV25-Bi method. From top to bottom, the waveforms of the speed $n$, electromagnetic torque $T_e$, phase current $i_a$ and $i_d$ are shown, respectively.

From the figure, we can see that when the motor operates at 360 r/min, the phase current waveform distortion of the VV13 method is more serious, indicating that the motor phase current contains more harmonic current. In addition, the motor speed and torque ripple are more serious

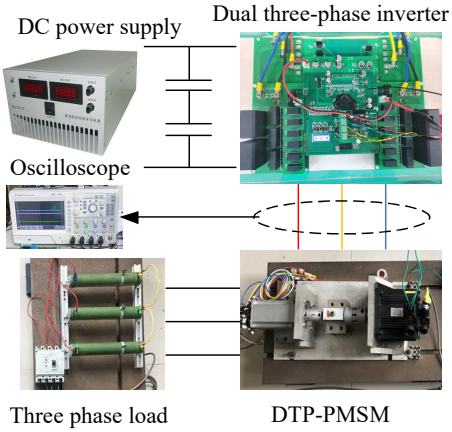


Fig. 10. Structure diagram of experimental platform

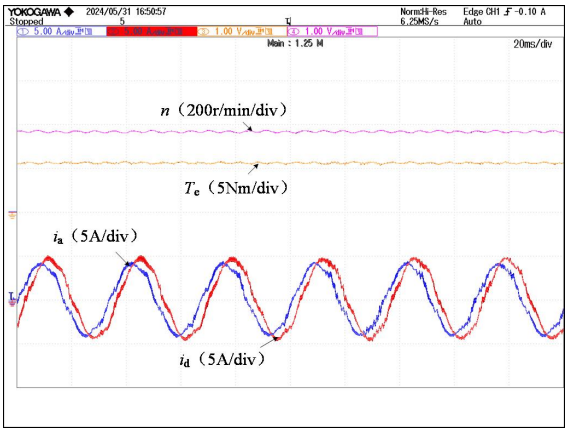


(a) VV13

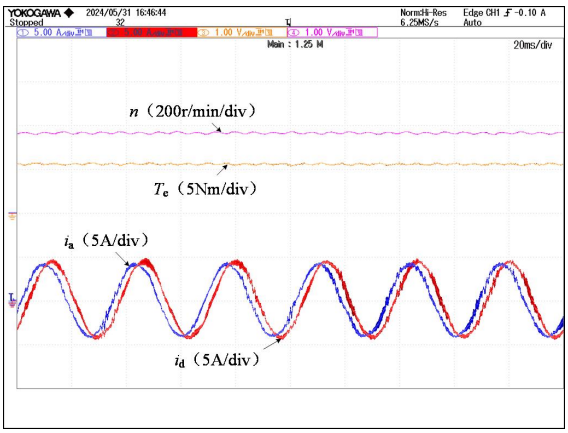


(b) VV25-Bi

Fig. 11. Motor experimental waveform at 360 r/min

than that of the VV25-Bi method. This is because the VV13 method only uses large and medium-large vectors to synthesize the prediction vector in the single-plane, and does not make full use of the motor voltage vector to suppress the harmonic current in the $x$–$y$ plane. Thus, larger harmonic current and torque ripple are formed. Under the VV25-Bi method, the phase current waveform is smoother, closer to the sine wave, and the motor speed and torque ripple are smaller, indicating that the phase current has less harmonic content and good stability.

In order to verify the dynamic performance of the motor, we verified the impact of a sudden load increase and decrease on the motor speed $n$, $T_e$ and phase current $i$. The experimental waveform is shown in Fig. 12. Figure 12(a) is a waveform diagram under the VV13 method, and Fig. 12(b) is a waveform diagram under the VV25-Bi method. From top to bottom, the waveforms of speed $n$, $T_e$, phase current $i_a$ and $i_d$ are shown respectively. From the figure, the VV13 and VV25-Bi methods have similar dynamic response with fast speed response, fast torque response, and less overshoot.

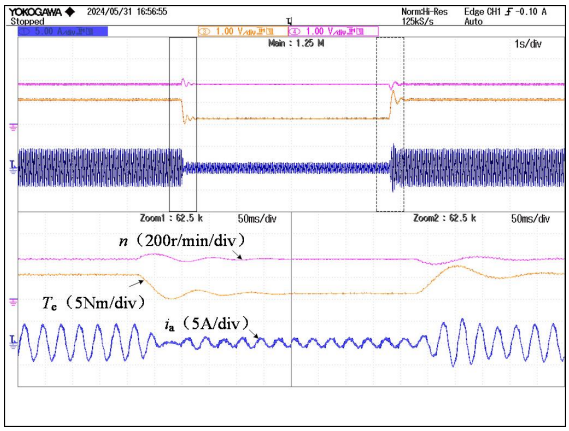


(a) VV13

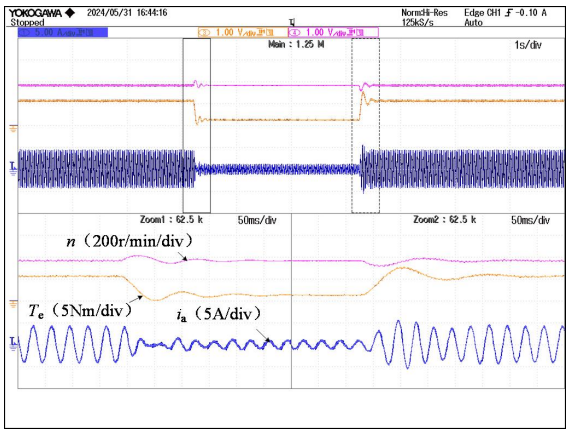


(b) VV25-Bi

Fig. 12. Waveform when increasing or decreasing load

To further verify the superiority of the proposed strategy under the condition that the phase current is 10 A, the 5th harmonic, 7th harmonic, total harmonic distortion (THD), and motor efficiency of VV13 and VV25-Bi are shown in Table 2 and Fig. 13.

Table 2. Performance comparison of the VV13 and VV25-Bi

| Control algorithm | THD | 5th harmonic | 7th harmonic | Motor efficiency |
|---|---|---|---|---|
| VV13 | 8.60% | 5.04% | 2.63% | 93.25% |
| VV25-Bi | 6.83% | 1.75% | 1.22% | 95.37% |

It can be seen from Table 2 and Fig. 13 that the THD of the proposed biplane MPC strategy is only 6.83%, lower than VV13. The 5th harmonic is only 1.75% and the 7th harmonic is only 1.22%, which are also significantly lower than VV13. It shows that the proposed strategy has stronger harmonic suppression performance. In addition, the DTP–PMSM efficiency of the proposed biplane MPC strategy is also higher than that of the VV13 MPC, because of the improved mover current quality.

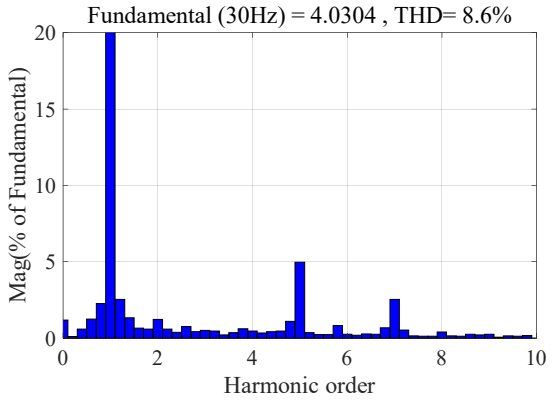


(a) VV13

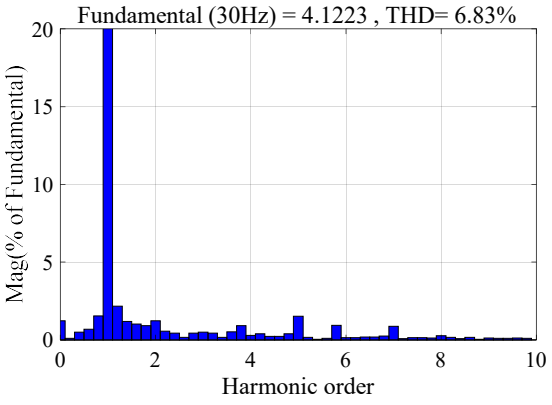


(b) VV25-Bi

Fig. 13. THD wave of different methods on the $\alpha$–$\beta$ plane

## 7. Conclusions

In this paper, the VV25-Bi MPC method based on the biplane virtual voltage vector is proposed to solve the shortcomings of the DTP–PMSM, such as high current harmonic content, large flux ripple and torque ripple. In the proposed VV25-Bi MPC, 25 virtual voltage vectors are synthesized in the $\alpha$–$\beta$ sub-plane and $x$–$y$ sub-plane for independent control in each plane, to suppress the harmonic current in the $x$–$y$ sub-plane, enhance the anti-interference ability of the motor, reduce the harmonic loss and torque ripple, and improve the operation performance of the DTP–PMSM system. Compared with the single-plane VV13 and VV25 MPC strategies, the proposed biplane VV25-Bi MPC strategy can better suppress the harmonic currents. The simulation model and experimental platform are designed. The simulation and experimental results verify the superiority of the proposed method, which has better control performance and can meet the high-performance control requirements of the DTP–PMSM.

## Acknowledgment

This work was supported in part by the Jiangsu Natural Science Foundation of China (Project No. BK20191225).

### References

[1] Liao W., Lyu M., Huang S., Wen Y., Shoudao H., *An Enhanced SVPWM Strategy Based on Vector Space Decomposition for Dual Three-Phase Machines Fed by Two DC-Source VSIs*, IEEE Transactions on Power Electronics, vol. 36, no. 8, pp. 9312–9321 (2021), DOI: 10.1109/TPEL.2021.3052913.

[2] Bu F., Yang Z., Gao Y., *Speed Ripple Reduction of Direct-Drive PMSM Servo System at Low-Speed Operation Using Virtual Cogging Torque Control Method*, IEEE Transactions on Industrial Electronics, vol. 68, iss. 1, pp. 160–174 (2020), DOI: 10.1109/TIE.2019.2962400.

[3] Kolano K.J., *Operation of a drive system using two independent PMSM motors in passenger lift door drives*, Archives of Electrical Engineering, vol. 68, no. 2, pp. 47–62 (2019), DOI: 10.24425/aee.2019.125979.

[4] Huang L.S., Zhao W.X., Ji J.H., Xue R., *Direct torque control of dual three-phase permanent magnet motor with improved steady-state performance*, IEEE Transactions of China Electrotechnical Society, vol. 37, no. 2, pp. 355–367 (2022), DOI: 10.19595/j.cnki.1000-6753.tces.200839.

[5] Hu Y.S., Li Y.G., Ma X.D., Li X.F., Huang S.D., *Flux-Weakening Control of Dual Three-Phase PMSM Based on Vector Space Decomposition Control*, IEEE Transactions on Power Electronics, vol. 36, no. 7, pp. 1428–1438 (2021), DOI: 10.1109/TPEL.2020.3044574.

[6] Tang H.Y., Sha O., Yang Z.L., Xu D.Z., *Deadbeat Two-vector model predictive current control for open-winding primary permanent-magnet linear motor*, Journal of Vibroengineering, vol. 24, no. 3, pp. 577–590 (2022), DOI: 10.21595/jve.2022.22248.

[7] Omran A.S., Hamad M.S., Abdelgeliel M., *An Adaptive Model Based on Data driven Approach for FCS-MPC Forming Converter in Microgrid*, International Journal of Control, Automation, and Systems, vol. 21, no. 11, pp. 3777–3795 (2023), DOI: 10.1007/s12555-022-0928-4.

[8] Gonçalves P.F.C., Cruz S.M.A., Mendes A.M.S., *Bi-subspace predictive current control of sixphase PMSM drives based on virtual vectors with optimal amplitude*, IET Electric Power Applications, vol. 13, no. 11, pp. 1672–1683 (2019), DOI: 10.1049/iet-epa.2019.0136.

[9] Zheng W., Chen Y., Wang X., *Fractional*: *Order Sliding Mode Control for Permanent Magnet Synchronous Motor Speed Servo System via an Improved Disturbance Observer*, International Journal of Control, Automation, and Systems, vol. 21, no. 4, pp. 1143–1153 (2023), DOI: 10.1007/s12555-021-0752-2.

[10] Liu S.Y., Liu CH., Huang Y.C., Xiao Y., *Direct Modulation Pattern Control for Dual Three-Phase PMSM Drive System*, IEEE Transactions on Industrial Electronics, vol. 69, no. 1, pp. 110–120 (2022), DOI: 10.1109/TIE.2021.3053880.

[11] Wróbel K., Szabat K., Serkies P., *Long-horizon model predictive control of induction motor drive*, Archives of Electrical Engineering, vol. 68, no. 3, pp. 579–593 (2019), DOI: 10.24425/AEE.2019.129343.

[12] Guo F., Yang T., Diab A.M., Yeoh S.S., Wheeler P., *An Enhanced Virtual Space Vector Modulation Scheme of Three-Level NPC Converters for More Electric Aircraft Applications*, IEEE Transactions on Industry Applications, vol. 57, no. 5, pp. 5239–5251 (2021), DOI: 10.1109/TIA.2021.3085798.

[13] Bermudez M., Arahal M.R., Duran M.J., Gonzalez-Prieto I., *Model Predictive Control of Six-Phase Electric Drives Including ARX Disturbance Estimator*, in IEEE Transactions on Industrial Electronics, vol. 68, no. 1, pp. 81–91 (2021), DOI: 10.1109/TIE.2019.2962477.

[14] Prieto I.G., Duran M.J., Aciego J.J., Barrero F., Martin C., *Model Predictive Control of Six-Phase Induction Motor Drives Using Virtual Voltage Vectors*, IEEE Transactions on Industrial Electronics, vol. 65, no. 1, pp. 27–37 (2018), DOI: 10.1109/TIE.2017.2714126.

[15] Aciego J.J., Priet I.G.O., Duran M.J., *Model Predictive Control Based on Dynamic Voltage Vectors for Six-Phase Induction Machines*, IEEE Journal of Emerging and Selected Topics in Power Electronics, vol. 9, no. 3, pp. 2710–2722 ( 2021), DOI: 10.1109/jestpe.2020.2977144.

[16] Luo Y.X., Liu C.H., *Elimination of Harmonic Currents Using a Reference Voltage Vector Based-Model Predictive Control for a Six-Phase PMSM Motor*, IEEE Transactions on Power Electronics, vol. 34, no. 7, pp. 6960–6972 (2019), DOI: 10.1109/TPEL.2018.2874893.

[17] Yu F., Liu X., Zhu Z.H., Mao J.F., *An Improved Finite-Control-Set Model Predictive Flux Control for Asymmetrical Six-Phase PMSMs with a Novel Duty-Cycle Regulation Strategy*, IEEE Transactions on Energy Conversion, vol. 36, no. 2, pp. 1289–1299 (2021), DOI: 10.1109/TEC.2020.3031067.

[18] Wang W., Liu C.H., Liu S., Zhao H., *Model Predictive Torque Control for Dual Three-Phase PMSMs with Simplified Deadbeat Solution and Discrete Space-Vector Modulation*, IEEE Transactions on Energy Conversion, vol. 36, no. 2, pp. 1491–1499 (2021), DOI: 10.1109/TEC.2021.3052132.

[19] Pandit J.K., Aware M., Nemade R., Yogesh T., *Simplified Implementation of Synthetic Vectors for DTC of Asymmetric Six-Phase Induction Motor Drives*, IEEE Transactions on Industry Applications, vol. 54, no. 3, pp. 2306–2318 (2018), DOI: 10.1109/TIA.2018.2789858.

[20] Luo Y.X., Liu C.H., *Model Predictive Control for a Six-Phase PMSM Motor with a Reduced-Dimension Cost Function*, IEEE Transactions on Industrial Electronics, vol. 67, no. 2, pp. 969–979 (2020), DOI: 10.1109/TIE.2019.2901636.

[21] Luo Y.X., Liu C.H., *Multi-Vector-Based Model Predictive Torque Control for a Six-Phase PMSM Motor with Fixed Switching Frequency*, IEEE Transactions on Energy Conversion, vol. 34, no. 3, pp. 1369–1379 (2019), DOI: 10.1109/TEC.2019.2917616.

[22] Wang X.Q., Wang Z., He M.Z., *Fault-Tolerant Control of Dual Three-Phase PMSM Drives with Minimized Copper Loss*, IEEE Transactions on Power Electronics, vol. 36, no. 11, pp. 12938–12953 (2021), DOI: 10.1109/TPEL.2021.3076509.

[23] Prieto I.G., Durán M.J., Bermúdez M., Barrero F., Martín C., *Assessment of Virtual Voltage-Based Model Predictive Controllers in Six-Phase Drives Under Open-Phase Faults*, IEEE Journal of Emerging and Selected Topics in Power Electronics, vol. 8, no. 3, pp. 2634–2644 (2020), DOI: 10.1109/JESTPE.2019.2915666.

[24] Yu F., Liu X., Zhu Z., *An Improved Finite-Control-Set Model Predictive Flux Control for Asymmetrical Six-Phase PMSMs with a Novel Duty-Cycle Regulation Strategy*, IEEE Transactions on Energy Conversion, vol. 36, no. 2, pp. 1289–1299 (2021), DOI: 10.1109/TEC.2020.3031067.